Editors' Suggestion

Identification of dopant site and its effect on electrochemical activity in Mn-doped lithium titanate

Harishchandra Singh,[1] Mehmet Topsakal,[2] Klaus Attenkofer,[3] Tamar Wolf,[4] Michal Leskes,[4] Yandong Duan,[5] Feng Wang,[5] John Vinson,[6] Deyu Lu,[2,*] and Anatoly I. Frenkel[1,7,*]

[1]*Department of Materials Science and Chemical Engineering, Stony Brook University, Stony Brook, New York 11794, USA*
[2]*Center for Functional Nanomaterials, Brookhaven National Laboratory, Upton, New York 11973, USA*
[3]*National Synchrotron Light Source II, Brookhaven National Laboratory, Upton, New York 11973, USA*
[4]*Department of Materials and Interfaces, Weizmann Institute of Science, Rehovot 76100, Israel*
[5]*Sustainable Energy Technologies Department, Brookhaven National Laboratory, Upton, New York 11973, USA*
[6]*Materials Measurement Science Division, National Institute of Standards and Technology, Gaithersburg, Maryland 20899, USA*
[7]*Chemistry Division, Brookhaven National Laboratory, Upton, New York 11973, USA*

(Received 24 September 2018; published 20 December 2018)

Doped metal oxide materials are commonly used for applications in energy storage and conversion, such as batteries and solid oxide fuel cells. The knowledge of the electronic properties of dopants and their local environment is essential for understanding the effects of doping on the electrochemical properties. Using a combination of x-ray absorption near-edge structure spectroscopy (XANES) experiment and theoretical modeling we demonstrate that in the dilute (1 at. %) Mn-doped lithium titanate ($Li_{4/3}Ti_{5/3}O_4$, or LTO) the dopant Mn^{2+} ions reside on tetrahedral (8*a*) sites. First-principles Mn K-edge XANES calculations revealed the spectral signature of the tetrahedrally coordinated Mn as a sharp peak in the middle of the absorption edge rise, caused by the $1s \rightarrow 4p$ transition, and it is important to include the effective electron-core hole Coulomb interaction in order to calculate the intenisty of this peak accurately. This dopant location can explain the impedance of Li migration through the LTO lattice during the charge-discharge process, and, as a result, the observed remarkable 20% decrease in electrochemical capacity of the 1% Mn-doped LTO compared to pristine LTO.

DOI: 10.1103/PhysRevMaterials.2.125403

I. INTRODUCTION

Understanding working mechanisms in functional nanomaterials (e.g. catalysts, electrocatalysts, battery and energy materials, actuators, etc.) at the atomistic level opens up opportunities for their rational design [1–4]. In many materials with advanced optical, magnetic, electronic, mechanical, and catalytic properties, functionalities arise due to changes in local environment and electronic structure with doping or substitution [5–10]. The AB_2O_4 type spinel lithium titanate ($Li_{4/3}Ti_{5/3}O_4$, or LTO) is a promising anode material for Li-ion batteries (LIBs). Owing to various attributes such as zero-strain, long cycle life, and relatively high potential range (1.5 V vs Li^+/Li) in the charge/discharge process, LTO has demonstrated outstanding cyclability and safety in high power LIBs over conventional graphitic anode materials [11–13]. Among several factors limiting the commercial use of LTO as anode material in LIBs is its poor electronic conductivity, restricting its rate capability [13]. Doping with various metals (such as Mg, V, Cr, Mn, Co, Ni, Cu, Zn, Y, etc.) has been broadly adopted by several groups as an efficient and effective way to increase electronic conductivity and therefore improve the rate capability of LTO [14–24]. However, enhanced electronic conductivity does not guarantee enhanced rate performance [14,24], and, indeed, dramatic variations in electrochemical properties on doping have been observed [11,25,26]. As an example of the ongoing debates in the case of Mn-doped LTO (referred to as Mn-LTO in this article), Doretta *et al.* [18] have reported reduced conductivity while Hulya *et al.* [19] have reported increased conductivity compared to the pristine LTO. Among other possible scenarios, these variations in the conductivity and related rate performances have been attributed to the different locations of dopants in LTO lattice and the impact on the Li ion diffusivity [15,16,18–22].

In pristine LTO, tetrahedral 8*a* sites are believed to be occupied by Li^+ ions, while the octahedral 16*d* sites are randomly occupied by Li^+ and Ti^{4+} ions with a 1:5 ratio [26]. Since Li^+ ions migrate through the LTO lattice via tetrahedral/octahedral sites, the occupancy of these sites by dopants should have an important effect on Li ion transport and thus electrochemical properties of LTO electrodes [8,9,11,27]. For example, the doping on the tetrahedral (8*a*) site is expected to be detrimental for Li ion conductivity due to the blocking of Li ion diffusion pathways [13]. However, the dopant location in LTO is a subject of debate. Earlier investigations suggest octahedral location for dopants [15–17,19–24]. Others have reported mixed (tetrahedral and octahedral) or tetrahedral coordination of dopants in LTO [18–21]. One important example is (1–30)% Mn-doped LTO, which has been a focus of several investigations [17–19]. In their experiments with 10% Mn-doped LTO, Doretta *et al.* [18] proposed tetrahedral Mn, while Hulya *et al.* [19] proposed octahedral Mn for the same concentration. In order to resolve the controversy on the dopant site in the doped LTO

*Authors to whom correspondence should be addressed: dlu@bnl.gov, anatoly.frenkel@stonybrook.edu

and its impact on electrochemical performance, it is important to establish a general and reliable methodology to provide local structural information around the dopant atom.

X-ray absorption near edge structure (XANES) spectroscopy is a premier technique for the purpose of dopant site identification, because it contains information about the local coordination geometry and electronic properties of a particular atomic species [28]. While XANES modeling is still a challenging problem in general, the progress achieved during the last decades in developing theoretical XANES codes enables the use of XANES for quantitative analysis of molecular and bulk compounds [29,30]. In this work we used theoretical modeling of XANES spectra of the Mn K-edge to identify the location of Mn dopants in the spinel LTO lattice. We correlate the Mn doping site with the substantial reduction of rate performance of Mn-doped LTO compared to the pristine LTO anode.

II. METHODS

A. Material Synthesis

The samples of pristine and 1 at. % Mn-doped LTO were prepared by solid state reactions as described previously [31]. The pristine and Mn-doped LTO samples were made in the same conditions and thus have similar granularity (Fig. S1). The details of their characterization by multiple complementary techniques and the results can be found elsewhere [31,32].

B. X-ray Absorption Spectroscopy Measurements

Mn K-edge (6540 eV) XANES measurements were performed at the ISS beamline of the National Synchrotron Light Source – II (NSLS-II) at Brookhaven National Laboratory. The sample powder was pressed into a pellet for the measurements at the Mn K-edge. The x-ray absorption coefficient data were measured in the fluorescence mode, using a multielement silicon drift detector (SDD). Twenty scans were averaged to improve the signal-to-noise ratio. For the purpose of comparison with the parent LTO, we collected Ti K-edge XANES data of Mn-doped LTO in the transmission mode (for this the powder was mixed with boron nitride to prepare a pellet) at the beamline BL2-2 at Stanford Synchrotron Radiation Lightsource (SSRL) at SLAC National Accelerator Laboratory. The Athena software from the DEMETER data analysis package [33] was used for the data alignment, merging, and normalization.

C. Electrochemical Measurements

For electrochemical measurements, electrodes were prepared by mixing 80 wt % active material (pristine and doped LTO powder, individually) with 10 wt % acetylene black and 10 wt % polyvinylidene fluoride (PVDF). A glass fiber GF/F (Whatman) filter was used as the separator and ethylene carbonate (EC)/dimethyl carbonate (DMC)/ LiPF6 (1:1:1) was used as the electrolyte. The 2032-type coin cells were assembled in an Ar glovebox, with metallic lithium foil (MIT Crop.) as the counter electrode. The discharge/charge measurements were carried out on an Arbin Instrument (BT−2400) test system at several different rates (0.2, 0.5, and 1 C) at ambient temperature (The C rate is a measure of current normalized by the battery's capacity, e.g., for a 1 Ah battery capacity 1 C = 1 A).

D. Computational Details

Ab initio simulations presented in this study consist of two steps. In the first step, structural relaxation of Mn-doped LTO was carried out within spin-polarized density functional theory (DFT) using projected augmented wave (PAW) potentials [34] as implemented in Vienna Ab Initio Simulation Package (VASP) package [35,36]. The exchange-correlation potential was evaluated under the generalized gradient approximation using the Perdew, Burke, and Ernzerhof (PBE) [37] functional. The kinetic energy cutoff of the plane-wave basis was chosen as 550 eV, and the Brillouin zone was sampled with a 4×4×2 Γ-centered grid. In order to improve the treatment of the strongly correlated 3*d* orbitals of Mn and Ti, the DFT + U method [38] was employed. The value of the effective Hubbard U parameter was chosen as 3 eV for both Mn and Ti ions as suggested by Capdevila-Cortada *et al.* [39]. A Gaussian broadening of 0.5 eV was chosen to plot the projected density of states (PDOS) using VASP.

In the second step, Mn K-edge XANES spectra were simulated for the optimized structures using the OCEAN package [40,41]. Ground state wave functions and orbital energies, which are input for OCEAN calculations, were obtained from plane-wave norm-conserving pseudopotential calculations under the local density approximation using the Quantum ESPRESSO package [42] with a kinetic energy cutoff of 100 Rydberg. The same Brillouin zone sampling and DFT+U treatment as in the previous step were used. The final state effects were included through the effective electron–core-hole interaction, treated by the Bethe-Salpeter equation [43]. A total of 1280 bands were included (up to 100 eV above the Fermi level) to compute the screened core-hole potential in the OCEAN calculations. Core-hole lifetime broadening was included using a fixed energy Lorentzian broadening applied on the computed spectra with a full width at half maximum (FWHM) of 1.1 eV [44]. In order to account for broadening by the excited state lifetimes, an additional variable energy Lorentzian broadening was applied [45–47]. The FWHM of Lorentzian broadening was chosen as $(E\text{-}E_{\text{onset}})/10$ with E_{onset} being the onset energy of the main edge of the calculated spectra.

III. RESULTS AND DISCUSSION

Figure S2 shows that the Mn-doped LTO electrode exhibits reasonable cycling stability at a low rate (0.2C). Discharge/charge at different rates were also performed both on pristine LTO and Mn-doped LTO electrodes and the voltage profiles are presented in Figs. 1(a)–1(c). All the curves show that the insertion/extraction of Li ions into/out of the LTO framework occurs at stable potential plateaus of 1.54 V (discharge) and 1.58 V (charge) vs Li^+/Li^0. Despite that specific capacity decreases with increasing C rate in both types of LTO electrodes, the capacity of pristine LTO is significantly higher than that of doped LTO at the same C rates

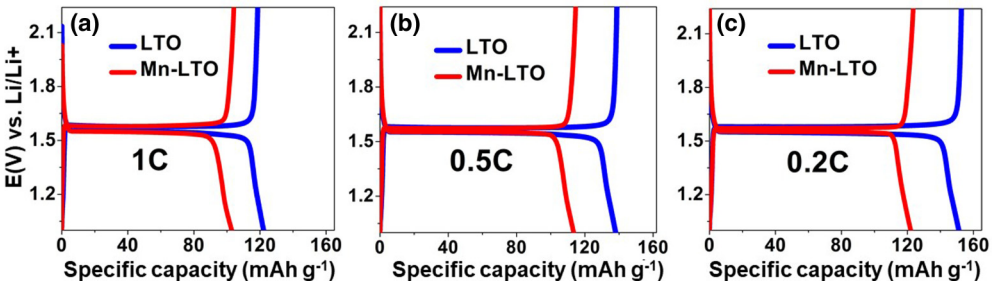

FIG. 1. Voltage profiles during discharge/charge for pristine LTO and Mn-doped LTO. The electrochemical measurements were performed at three different rates, 1C (a), 0.5C (b), and 0.2C (c), in the voltage range between 1.0 and 2.2 V (vs Li/Li+); see also cycling performance in the Supplemental Material (Fig. S2).

[Figs. 1(a)–1(c)]. Our electrochemical measurements demonstrate the maximum capacity of 150 mA hg^{-1} for pristine LTO [Fig. 1(c)], which is reasonably high considering the large size of the particles (in the micron range – see Supplemental Material [48] for more details) and comparable to other reports, generally ranging from 140 to 160 mA hg^{-1} at similar rate of 0.2C as compared to a theoretical specific capacity of 175 mA hg^{-1} [13]. In Mn-LTO, the specific capacity at 0.2C is reduced to ∼122 mA hg^{-1}, which is nearly a 20% decrease compared to the pristine LTO [Fig. 1(c)]. Such a large capacity drop in the 1% Mn-doped sample is intriguing, because it cannot be attributed to the difference in grain size or morphology, as both samples were synthesized by the same method and thus have the similar granularity (Supplemental Material [48]). In search of a possible explanation for this puzzling behavior, in the following sections we investigate the dopant sites of Mn atoms in LTO by a combination of XANES spectroscopy and theoretical modeling.

Due to the complexity in the Li/Ti site occupation (e.g., multiple sites with different local symmetries and the randomness in the occupancy of the 16*d* site), identifying the site of the dopant atom in LTO is a difficult task. In our previous study [49], following Ziebarth *et al.* [50], we modeled the atomic structure of LTO using a hexagonal supercell containing two chemical formula equivalents of $Li_4Ti_5O_{12}$ as presented in Fig. 2. This model was chosen to construct a minimum super cell for computational efficiency that satisfies

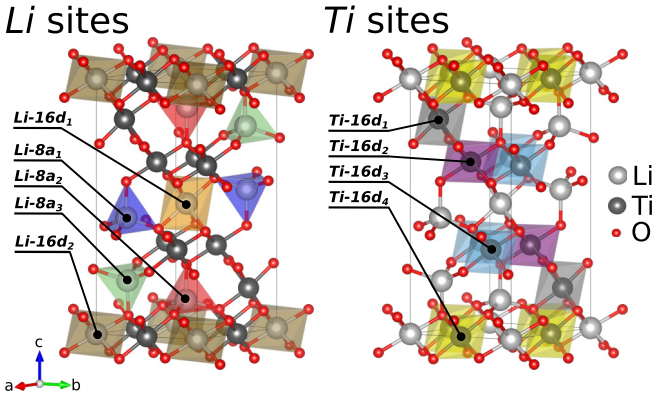

FIG. 2. Atomic structure of spinel lithium titanate (LTO) in the hexagonal unit cell. Inequivalent Li (left) and Ti (right) sites are denoted by different colors.

the correct stoichiometry at the 16*d* sites with a 1:5 Li to Ti molar ratio. The most stable configuration was found to correspond to the largest distance between Li ions at 16*d* sites such that the electrostatic repulsion is minimized [50]. Because of translational and rotational symmetry, some Li and Ti sites are equivalent in the structural model. Inequivalent Li and Ti sites are presented in Fig. 2 with different colors. Li ions at 16*d* sites are sixfold coordinated in the octahedral environment, while Li ions at 8*a* sites are fourfold coordinated in the tetrahedral environment. Li sites can be classified into five types labeled Li-16d_1, Li-16d_2, Li-8a_1, Li-8a_2, and Li-8a_3. All Ti sites in LTO are octahedrally coordinated. Four inequivalent Ti sites are labeled Ti-16d_1, Ti-16d_2, Ti-16d_3, and Ti-16d_4. In addition to 16*d* and 8*a* sites, there are empty 16*c* sites in LTO (not shown in Fig. 2) that are six coordinated and located in between two Li-8*a* sites. Li ions at 8*a* sites migrate to the 16*c* sites during Li intercalation, while the locations of Ti-16*d* ions remain unaffected. When pristine LTO is doped with Mn atoms, it is expected that Mn ions will replace one of Li or Ti ions at 16*d* and 8*a* sites (as shown in Fig. 2) or fill an empty 16*c* site. The identification of the Mn dopant site from the experiment is extremely challenging due to the difficulty in extracting atomic scale information and the multiple possible doping sites for Mn, some or all of which can be occupied. XANES spectroscopy is a premier method for locating the dopant site, due to its chemically specific sensitivity to local coordination environment and charge state of dopants [51–53]. In previous work by us and others, XANES studies of many types of dopants were used to identify their location in the host structure [54–56]. Determination of the local atomic environment from given sets of XANES data is an inverse problem of modeling and cannot be solved easily. Hence, we present our analysis in detail, starting from the analysis of the raw data, followed by the computational modeling of possible Mn dopants sites in LTO, to identify the site showing the best agreement between theory and our experiment.

A typical transition metal K-edge XANES spectrum provides the information on the oxidation state, electronic charge state, and local coordination of the absorber [53]. In the literature, energy position of the main absorption edge is defined either as the energy corresponding to the half of the absorption edge step height, the energy of the maximum of the absorption peak, or the first inflection point. The energy position may shift because of many factors such as the change

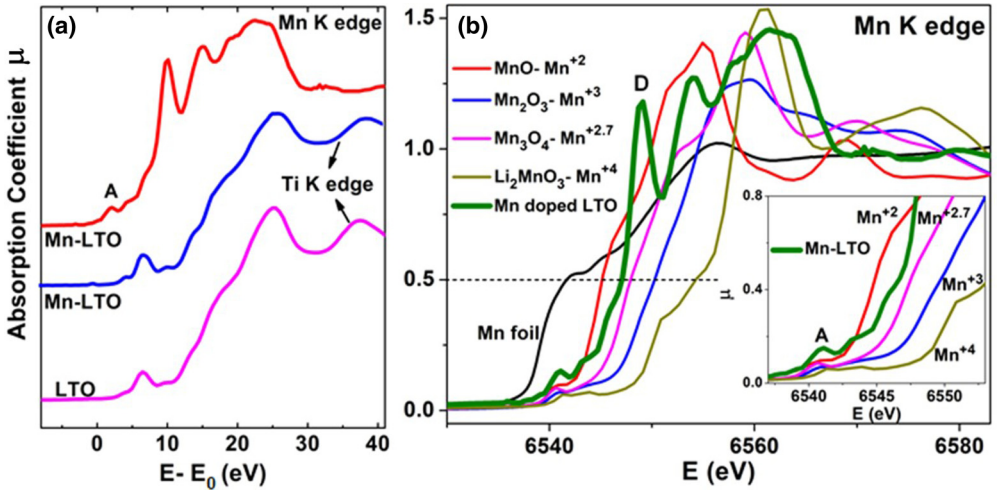

FIG. 3. (a) Normalized K-edge XANES spectra of Mn and Ti edges in the pristine and Mn-doped LTO samples plotted versus photoelectron energy E-E_0, where E_0 is the ionization energy of the 1s electron for Ti (4965 eV) and Mn (6540 eV). (b) Edge step normalized Mn K-edge XANES spectra of doped LTO sample along with Mn standards such as MnO, Mn_2O_3, Mn_3O_4 and Li_2MnO_3 are also shown. Mn foil spectrum is used for photon energy calibration. The inset shows the enlarged pre-edge.

in the oxidation state, bond covalency, the nature of the ligands, coordination numbers, and electronegativity of the anion [57–59]. Figure 3 shows the edge step normalized K-edge XANES spectra of pristine and Mn-doped LTO sample at the Ti and Mn edges. The Ti K-edge XANES spectrum of Mn-doped LTO does not show any visible change compared to the pristine LTO [Fig. 3(a)], consistent with Ti remaining in the Ti^{4+} state [49].

We will now focus on the Mn K-edge XANES data [Fig. 3(b)]. Together with the Mn-doped LTO sample, we have plotted spectra of Mn standards such as MnO (Mn^{2+}), Mn_2O_3 (Mn^{3+}), Mn_3O_4 ($Mn^{2+/3+}$), and Li_2MnO_3 (Mn^{4+}). To characterize the oxidation state of Mn in LTO, we compare the position of its XANES spectrum at the 0.5 edge step level with those in the standard compounds. That comparison places the oxidation state of Mn in LTO between, approximately, 2+ and 2.7+, consistent with independent electron paramagnetic resonance (EPR) results showing Mn to be in the 2+ state in the same material [32].

As shown in Fig. 3(b) (inset) the pre-edge feature A for Mn-doped LTO is the highest with respect to the standards. This effect is an indication of the less symmetric environment, on average, of Mn in LTO compared to those in standard compounds. As shown in Fig. 2, the Mn dopant can occupy either octahedral (Ti/Li-16d and 16c) or tetrahedral (Li-8a) sites in LTO. Also, based on previous reports on the standards used, Mn atoms exist either in (regular or distorted) octahedral geometry (in MnO, Mn_2O_3, Li_2MnO_3) or mixed (tetrahedral as well as octahedral) coordination geometry (in Mn_3O_4), which result in different peak heights in their pre-edge region [see the inset of Fig. 3(b)] [58,59]. There are other compounds such as $YMnO_3$, YMn_2O_5, and $Li_4Mn_2O_5$ where Mn has also been reported to be in trigonal bipyramidal, square pyramidal and spherically distorted octahedral coordination [60–62]. We assign peak A to the dipole-forbidden $s \rightarrow d$ transition. A finite peak intensity can arise from either the Mn 3d-4p hybridization or Mn 3d to ligand O 2p mixing, when the local symmetry is lowered by the distortion of the polyhedron [51,63,64]. Therefore, based on the pre-edge features, we conclude that the Mn environment is distorted from the ideal octahedral one. However, from this observation alone, we cannot discriminate between the two possible scenarios: (a) the strongly distorted octahedral environment of the Ti/Li-16d and 16c site or (b) the tetrahedrally coordinated Li-8a site. A mixed site placement may also explain the data. Because of the limitations of such a qualitative approach to XANES interpretation, we also performed theoretical XANES calculations.

Based on the structural model of LTO shown in Fig. 2, we investigated the energetics of Mn doping in various possible sites with DFT total energy calculations. The pristine LTO structure contains 8 Li, 10 Ti, and 24 O atoms in the unit cell. We first looked at Li substitution and compared ground state total energies of fully relaxed Mn-LTO structures for all possible Mn-doping configurations as shown in Fig. 2. The Li-8a_3 site [Fig. 2(a)] turned out to be the most stable Li site for Mn substitution. The Li-8a_2, Li-8a_1, Li-16d_1, and Li-16d_2 sites are 132, 205, 270, and 421 meV higher in energy for Mn substitution. This analysis was also performed for Ti sites [Fig. 2(b)]. When one of the Ti ions is replaced with Mn, it corresponds to 10% Mn substitution. Based on total energy calculations, the Ti-16d_2 site is the energetically most favorable Ti site for Mn substitution. Total energies of Mn substitution at Ti-16d_1, Ti-16d_3, and Ti-16d_4 with respect to Ti-16d_2 site are 19, 30, and 56 meV higher. Because of the large number of possible 16c interstitial sites for Mn, we performed the calculation on a representative configuration.

For the Li-8a_3 site, which is the energetically most favorable configuration among Li sites, our calculation yields a high total magnetization of 6.0 μ_B per unit cell. This high-spin state can be interpreted as Mn ion in the 2+ charge state with all 3d orbitals half occupied (five spin-up) according to Hund's rule. We considered several scenarios for distributing the extra electron density (caused by the substitution of Li^+ by Mn^{2+}). The results for the Mn XANES spectrum were indistinguishable for the two spin configurations we considered: (1) one Ti^{4+} ion was reduced to Ti^{3+} and (2) the electron

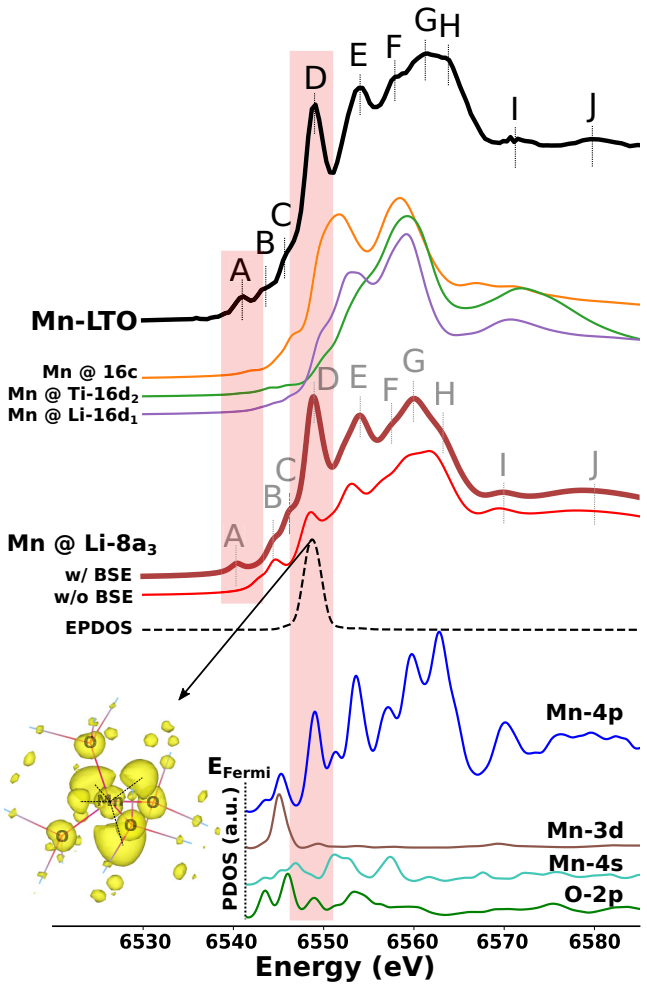

FIG. 4. Comparison of calculated XANES spectra of Mn K-edge for several Mn absorption sites with experimental spectrum. Major features in the spectra are labeled by letters A–J. Electron-hole wave function corresponding to peak D is shown in the isosurface plot. PDOS of the Mn at Li-8a_3 site and four oxygen atoms surrounding Mn are aligned with corresponding XANES. Fermi level was set to the minimum of conduction bands.

density was delocalized among all Ti ions in the unit cell. On the other hand, replacing Ti-16d_2 with Mn simply leads to the formation of Mn^{4+} with remaining three *3d* electrons half occupying t_{2g} orbitals. As a result, the system has an intermediate magnetization of 3.0 μ_B per unit cell.

Next, we performed Mn K-edge XANES simulations for Mn-doped at Li-8a_3, Li-16d_1, Ti-16d_2, and 16c sites and compared them with the experimental XANES spectrum. XANES spectra were calculated using the OCEAN package, which treats the electron-core hole interactions explicitly by solving the Bethe-Salpeter equation (BSE) [40,41]. OCEAN spectra calculated for Mn ions placed at 16c, Ti-16d_2, and Li-16d_1 octahedral sites apparently lack XANES pre-edge feature "A" as highlighted in rectangular area in Fig. 4. The calculated main edge features are also clearly different from experimental Mn-LTO spectrum. On the other hand, excellent agreement between computational XANES of the Mn ion placed at Li-8a_3 site and experimental Mn-LTO XANES is observed as shown in Fig. 4. In addition, the Mn^{2+} state at the Li-8a_3 site is consistent with the EPR results. Based on total energy calculations and XANES simulations, we conclude that Mn doping in LTO happens through the substitution of the Li at the 8a site.

Finally, we analyzed the XANES spectrum of Mn-LTO in more detail. Distinct peaks are visible in the spectrum, and we label them by letters (A through J) as shown in Fig. 4. To identify effects of core-hole interactions, the spectrum of Li-8a_3 calculated without BSE is also shown in Fig. 4 for comparison. In order to reveal origins of main edge peaks labeled D–J, we further calculated PDOS of Mn-doped LTO at Li-8a_3 site as shown at the bottom of Fig. 4. Except for some variations in the intensities, features labeled D–J are all present in the spectrum without BSE. From the correlation between Mn-p PDOS and the calculated XANES, we can clearly see that features labeled D through J originate from mostly $1s \rightarrow 4p$ transitions. On the other hand, features labeled A and C disappear in the absence of core-hole interactions (without BSE), as the electron–core-hole interaction modifies the oscillator strength significantly in the pre-edge region. A closer look at the PDOS of Mn 3d states in the conduction region (Fig. 4) reveals hybridization of the Mn 3d states with 4p states. We assign feature A to the $1s \rightarrow 3d$ transition which is dipole forbidden but is activated because of contributions from Mn 3d and 4p hybridization. O 2p states have substantial contribution to the low energy side of the spectrum below 6560 eV.

Peak D is a distinct feature of Mn-LTO as shown in Fig. 3(b), which is absent in the Mn K-edge of other standards. In order to gain further insights into this peak, we investigated its charge density distribution in both spatial and energy domain. For a given core electron excitation (S), the two-body electron-hole wave function can be expressed as

$$\chi^S(\boldsymbol{r_e}, \boldsymbol{r_h}) = \sum_{\boldsymbol{k}} \sum_{c} A^S_{c\boldsymbol{k}} \psi_{c\boldsymbol{k}}(\boldsymbol{r_e}) \psi^*_{1s,\boldsymbol{k}}(\boldsymbol{r_h}), \qquad (1)$$

where $\psi^*_{1s,\boldsymbol{k}}$, $\psi_{c\boldsymbol{k}}$, and $A^S_{c\boldsymbol{k}}$ are the Mn 1s core hole wave function, electron wave function of wave vector $\boldsymbol{k}$ in the conduction bands, and the eigenvectors of the excitation S, respectively. For a localized core hole at the Mn atom, the real space charge density is given by $|\chi^s(\boldsymbol{r_e}, \boldsymbol{r_h} = \boldsymbol{\tau_{Mn}})|^2 = |\sum_{\boldsymbol{k}} \sum_c A^S_{c\boldsymbol{k}} \psi_{c\boldsymbol{k}}(\boldsymbol{r_e})|^2$, where $\boldsymbol{\tau_{Mn}}$ is the ionic position of the excited Mn atom, and averaged over the polarization directions. We further introduce the excitation-projected density of states (EPDOS) to capture the charge density distribution in the energy domain, which is defined as

$$\mathrm{EPDOS}(S, E) = \sum_{\boldsymbol{k}} \sum_{c} \left|A^S_{c\boldsymbol{k}}\right|^2 \delta(E - E_{c\boldsymbol{k}}), \qquad (2)$$

where $E_{c\boldsymbol{k}}$ is the orbital energy of the empty state $\psi_{c\boldsymbol{k}}$. The charge density isosurface of peak D is shown in Fig. 4.

Locally the shape and orientation of the charge density on the Mn exhibit sp^3 hybrid orbitals in a tetrahedral arrangement, which is indicated by dashed black lines connecting four blobs with the one centered on the Mn. These unoccupied orbitals avoid the tetrahedral Mn-O bonds, pointing into the interstitial. Polarization-averaged EPDOS of peak D is shown

in Fig. 4 in the dashed line with a Gaussian broadening of $\sigma = 0.5$ eV. As highlighted by the rectangular area, it is well localized within the energy range of approximately 5 eV and contains pronounced Mn 4*p* contributions and significant Mn 4*s* and O 2*p* contributions. Although peak D is already present in the site-specific Li-8a_3 spectrum without BES, the peak intensity is significantly underestimated, which highlights the importance of including the electron-core hole screened Coulomb interaction in the simulated Mn XANES spectra. Another important feature of peak D is that the wave function of the excited electron is extended beyond O 2*p* orbitals in the nearest-neighbor shell, as one can clearly see even longer range contributions from Ti 3*d* orbitals and 2*p* orbitals of nonbonded oxygen atoms (see Supplemental Material [48]) at a lower isovalue than that in Fig. 4.

The charge density analysis indicates that peak D is characteristic of the tetrahedral Mn, which is absent in the Mn K-edge standards with pure six-coordinated Mn in Fig. 3(b), except for Mn_3O_4 with mixed Mn tetrahedral (1/3) and octahedral (2/3) occupancies. We further investigated XANES spectrum of Mn_3O_4. As shown in Fig. 3(b), Mn_3O_4 lacks spectral feature D although it has tetrahedral sites. Comparison of the experimental XANES spectrum at the Mn K-edge of Mn_3O_4 with those for site-specific and site-averaged spectra is presented in Supplemental Material [48]. Although peak D is missing in Mn_3O_4 XANES, the theoretically calculated site-specific XANES spectrum of tetrahedral site of Mn_3O_4 closely resembles the Mn K-edge of Mn-LTO with a well-defined peak D. The absence of the peak D in the site-averaged spectrum is a consequence of the predominance of the octahedral sites of Mn_3O_4 in the averaged spectrum. This analysis strengthens our claim that peak D is a characteristic spectral fingerprint of tetrahedrally coordinated Mn.

Based on the combination of experimental and theoretical XANES spectroscopy results we pinpointed the tetrahedral Mn site location in the LTO lattice, which can affect Li ion diffusivity. Li ion diffusion in LTO is an intriguing topic that has attracted extensive research efforts in recent years. Schmidt *et al.* [65] reported steep Li diffusivity increase during lithiation at the low charging stage in the NMR measurement. This remarkable behavior was attributed to the role of Li-16*d* in stabilizing the subnanometer phase boundary featuring Li-8*a*/Li-16*c* face-sharing local motifs [66]. The significance of the Li-8*a*/Li-16*c* face-sharing local motif in the rate performance of LTO was further supported by *in situ* Ti K-edge XANES analysis [49]. Furthermore, Reuter *et al.* observed Ti antisite-like defects stabilized by the configurational disorder in molecular dynamic simulations, which are characterized by a displacement of a Ti ion from a 16*d* to a 16*c* site and a shift of the Li ion on an adjacent 8*a* to the original 16*d* site [67]. A fast, local, and correlated Li ion diffusion was believed to be a key element in the sudden rise of the Li conductivity at the early stage of charging [67].

Our Mn K-edge XANES modeling identified the Li-8*a* site as the Mn doping site. This atomic level structural information can be qualitatively correlated with the significant (∼20%) rate performance drop in several ways that we outline here (more detailed, quantitative modeling is beyond the scope of this work). First, the large Mn^{2+} ion at the tetrahedral 8*a* site can partially block the Li interstitial diffusion pathway. Mn doping decreases available Li sites for Li diffusion. Similar effects have been observed in Mg-doped LTO, where the occupation of the 8*a* sites by Mg retards Li ion diffusion, lowers the gravimetric capacity, and reduces the electrochemical reversibility of the reaction [14]. It is likely that Mn dopant at the 8*a* site can quench the Ti antisite defects, which is detrimental to the fast local Li diffusion around the empty 8*a* sites in the Ti antisite defects. In addition, Mn may create local strain defects that can strongly affect Li transport, in analogy with the significant V-V bond stretching found in ∼1% Cr doped V_2O_3 [68].

IV. CONCLUSIONS

Using a combination of x-ray absorption near-edge structure experiment and theoretical spectroscopy modeling we demonstrated that Mn^{2+} ions in 1% Mn-doped LTO occupy tetrahedral (8*a*) sites. As a result, Mn ions may partially block the Li diffusion pathway and quench the Ti antisite defects, adversely affecting the rate performance of LTO. The latter was found experimentally to be 20% lower than in pristine LTO prepared under the same conditions. Our results explain the observation of decreased electrochemical activity in Mn-doped LTO qualitatively and provide directions for further modeling of Li ion transport and electrochemical activity. This same method can be used in the future for systematic analyses of other dopants and different battery materials in a broad concentration range. We also revealed a spectroscopic fingerprint of tetrahedrally coordinated Mn which may be useful for characterization and to guide design of Mn-based LTO battery materials.

ACKNOWLEDGMENTS

A.I.F. and H.S. acknowledge support by National Science Foundation (NSF) Grant No. DMR-1701747. This research used the 8-ID (ISS) beamline of the National Synchrotron Light Source, a US Department of Energy (DOE) Office of Science User Facility operated for the DOE Office of Science by Brookhaven National Laboratory under Contract No. DE-AC02-98CH10886. Operations at the Beamline BL2-2 in SSRL were supported in part by the Synchrotron Catalysis Consortium (US Department of Energy, Office of Basic Energy Sciences, Grant No. DE-SC0012335). The x-ray absorption spectra calculations used resources of the National Energy Research Scientific Computing Center (NERSC), a US Department of Energy Office of Science User Facility operated under Contract No. DE-AC02-05CH11231. Research was carried out at the Center for Functional Nanomaterials and the Scientific Data and Computing Center, a component of the Computational Science Initiative, which are supported by the US Department of Energy, Office of Basic Energy Sciences, under Contract No. DE-SC0012704. M.T. was supported by the LDRD grant at the Brookhaven National Laboratory (Grant No. 16–039). Efforts on electrochemical tests were supported by the Center for Mesoscale Transport Properties, an Energy Frontier Research Center supported by the U.S. Department of Energy (DOE), Office of Science, Basic Energy Sciences, under Award No. DE-SC0012673.

H.S. and M.T. contributed equally to this work.

[1] M. A. Newton, Catalysts **7**, 1 (2017).
[2] K. W. Chapman, MRS Bull. **41**, 231 (2016).
[3] W. Li, A. Wei, X. Li, L. Zhang, H. Wang, W. Ge, and Z. Liu, Int. J. Electrochem. Sci. **12**, 2822 (2017).
[4] J. Sun, J. Wu, X. Tong, F. Lin, Y. Wang, and Z. M. Wang, Adv. Sci. **5**, 1700780 (2018).
[5] Y. Amit, Y. Li, A. I. Frenkel, and U. Banin, ACS Nano **9**, 10790 (2015).
[6] J. Liu, Y. Amit, Y. Li, A. M. Plonka, S. Ghose, L. Zhang, E. A. Stach, U. Banin, and A. I. Frenkel, Chem. Mater. **28**, 8032 (2016).
[7] Z. Zhang, X. Liu, J. Yu, Y. Hang, Y. Li, Y. Guo, Y. Xu, X. Sun, J. Zhou, and W. Guo, Wiley Interdiscip. Rev. Comput. Mol. Sci. **6**, 324 (2016).
[8] R. Korobko, A. Patlolla, A. Kossoy, E. Wachtel, H. L. Tuller, A. I. Frenkel, and I. Lubomirsky, Adv. Mater. **24**, 5857 (2012).
[9] R. Korobko, A. Lerner, Y. Li, E. Wachtel, A. I. Frenkel, and I. Lubomirsky, Appl. Phys. Lett. **106**, 042904 (2015).
[10] P. Müller and I. Hermans, Ind. & Eng. Chem. Res. **56**, 1123 (2017).
[11] L. Zhao, Y.-S. Hu, H. Li, Z. Wang, and L. Chen, Adv. Mater. **23**, 1385 (2011).
[12] T.-F. Yi, S.-Y. Yang, and Y. Xie, J. Mater. Chem. A **3**, 5750 (2015).
[13] T. Yuan, Z. Tan, C. Ma, J. Yang, Z.-F. Ma, and S. Zheng, Adv. Energy Mater. **7**, 1601625 (2017).
[14] C. H. Chen, J. T. Vaughey, A. N. Jansen, D. W. Dees, A. J. Kahaian, T. Goacher, and M. M. Thackeray, J. Electro. Soc. **148**, A102 (2001).
[15] Z. Yu, X. Zhang, G. Yang, J. Liu, J. Wang, R. Wang, and J. Zhang, Electrochim. Acta **56**, 8611 (2011).
[16] H. Song, T.-G. Jeong, S.-W. Yun, E.-K. Lee, S.-A. Park, and Y.-T. Kim, Sci. Rep. **7**, 43335 (2017).
[17] P. Kubiak, A. Garcia, M. Womes, L. Aldon, J. O. Fourcade, P. E. Lippens, and J. C. Jumas, J. Power Sources **119**, 626 (2003).
[18] D. Capsoni, M. Bini, V. Massarotti, P. Mustarelli, G. Chiodelli, C. B. Azzoni, M. C. Mozzati, L. Linati, and S. Ferrari, Chem. Mater. **20**, 4291 (2008).
[19] H. Kaftelen, M. Tuncer, S. Tu, S. Repp, H. Göçmez, R. Thomann, S. Weber, and E. Erdem, J. Mater. Chem. A **1**, 9973 (2013).
[20] D. Capsoni, M. Bini, V. Massarotti, P. Mustarelli, S. Ferrari, G. Chiodelli, M. C. Mozzati, and P. Galinetto, J. Phys. Chem. C **113**, 19664 (2009).
[21] C. Lin, M. O. Lai, L. Lu, H. Zhou, and Y. Xin, J. Power Sources **244**, 272 (2013).
[22] D. Wang, H.-Y. Xu, M. Gu, and C.-H. Chen, Electrochem. Commun. **11**, 50 (2009).
[23] D. Wu and Y. Cheng, Ionics **19**, 395 (2013).
[24] Y.-J. Bai, C. Gong, N. Luna, and Y.-X. Qi, J. Mater. Chem. A **1**, 89 (2013).
[25] M. Armand and J. M. Tarascon, Nature (London) **451**, 652 (2008).
[26] T. Ohzuku, A. Ueda, and N. Yamamoto, J. Electrochem. Soc. **142**, 1431 (1995).
[27] H. Singh, D. Donetsky, J. Liu, K. Attenkofer, B. Cheng, J. R. Trelewicz, I. Lubomirsky, E. Stavitski, and A. I. Frenkel, Rev. Sci. Instrum. **89**, 045111 (2018).
[28] J. Stöhr, *NEXAFS Spectroscopy*, Springer Series in Surface Sciences (Springer-Verlag, Berlin, Heidelberg, 1992), Vol. 25.
[29] J. J. Kas, K. Jorissen, and J. J. Rehr, in *X-Ray Absorption and X-Ray Emission Spectroscopy: Theory and Applications*, edited by J. A. van Bokhoven and C. Lamberti (Wiley, New York, 2016).
[30] J. J. Rehr and A. L. Ankudinov, Coord. Chem. Rev. **249**, 131 (2005).
[31] T. Chakrabrty, N. Goldin, A. Feintuch, L. Houben, and M. Leskes, Chem. Phys. Chem. **19**, 1 (2018).
[32] T. Wolf, S. Kumar, H. Singh, T. Chakrabarty, F. Aussenac, A. I. Frenkel, D. T. Major, and M. Leskes, J. Am. Chem. Soc. (2018), doi: 10.1021/jacs.8b11015.
[33] B. Ravel and M. Newville, J. Synch. Radiat. **12**, 537 (2005).
[34] G. Kresse and D. Joubert, Phys. Rev. B **59**, 1758 (1999).
[35] G. Kresse and J. Hafner, Phys. Rev. B **47**, 558 (1993).
[36] G. Kresse and J. Hafner, Phys. Rev. B **49**, 14251 (1994).
[37] J. P. Perdew, K. Burke, and M. Ernzerhof, Phys. Rev. Lett. **77**, 3865 (1996).
[38] S. L. Dudarev, G. A. Botton, S. Y. Savrasov, C. J. Humphreys, and A. P. Sutton, Phys. Rev. B **57**, 1505 (1998).
[39] M. Capdevila-Cortada, Z. Łodziana, and N. López, ACS Catal. **6**, 8370 (2016).
[40] K. Gilmore, J. Vinson, E. L. Shirley, D. Prendergast, C. D. Pemmaraju, J. J. Kas, F. D. Vila, and J. J. Rehr, Comp. Phys. Commun. **197**, 109 (2015).
[41] J. Vinson, J. J. Rehr, J. J. Kas, and E. L. Shirley, Phys. Rev. B **83**, 115106 (2011).
[42] P. Giannozzi, S. Baroni, N. Bonini, M. Calandra, R. Car, C. Cavazzoni, D. Ceresoli, G. L. Chiarotti, M. Cococcioni, and I. Dabo *et al.*, J. Phys.: Condens. Matter **21**, 395502 (2009).
[43] E. E. Salpeter and H. A. Bethe, Phys. Rev. **84**, 1232 (1951).
[44] R. F. Egerton, Micron **34**, 127 (2003).
[45] J. L. Campbell and T. Papp, At. Data Nucl. Data Tables **77**, 1 (2007).
[46] C. Hébert, Micron **38**, 12 (2007).
[47] B. Ravel, A. J. Kropf, D. Yang, M. Wang, M. Topsakal, D. Lu, M. C. Stennett, and N. C. Hyatt, Phys. Rev. B **97**, 125139 (2018).
[48] See Supplemental Material at http://link.aps.org/supplemental/10.1103/PhysRevMaterials.2.125403 for information on the cyclic performance (Mn-doped $Li_{4/3}Ti_{5/3}O_4$) and SEM images for micron-sized pristine and doped samples. Electron-hole wave function isosurface and comparison of the experimental and theoretical XANES spectra in Mn-LTO and Mn_3O_4 samples are shown as well.
[49] W. Zhang, M. Topsakal, C. Cama, C. J. Pelliccione, H. Zhao, S. Ehrlich, L. Wu, Y. Zhu, A. I. Frenkel, K. J. Takeuchi, E. S. Takeuchi, A. C. Marschilok, D. Lu, and F. Wang, J. Am. Chem. Soc. **139**, 16591 (2017).
[50] B. Ziebarth, M. Klinsmann, T. Eckl, and C. Elsasser, Phys. Rev. B **89**, 174301 (2014).
[51] Z. Y. Wu, D. C. Xian, T. D. Hu, Y. N. Xie, Y. Tao, C. R. Natoli, E. Paris, and A. Marcelli, Phys. Rev. B **70**, 033104 (2004).
[52] H. Singh, H. Ghosh, T. V. C. Rao, A. K. Sinha, and P. Rajput, J. Appl. Phys. **116**, 214106 (2014).
[53] F. de Groot, G. Vanko, and P. Glatzel, J. Phys.: Condens. Matter. **21**, 104207 (2009).

[54] J. Timoshenko, A. Shivhare, R. W. J. Scott, D. Lu, and A. I. Frenkel, Phys. Chem. Chem. Phys. **18**, 19621 (2016).
[55] O. Elimelech, J. Liu, A. M. Plonka, A. I. Frenkel, and U. Banin, Angew. Chem. Int. Ed. **56**, 10335 (2017).
[56] K. Rammutla, S. L. P. Savin, M. G. Marshaba, A. V. Chadwick, and P. E. Ngoepe, Phys. Status Solidi C **4**, 765 (2007).
[57] C. Bressler, C. Milne, V.-T. Pham, A. ElNahhas, R. M. van der Veen, W. Gawelda, S. Johnson, P. Beaud, D. Grolimund, M. Kaiser, C. N. Borca, G. Ingold, R. Abela, and M. Chergui, Science **323**, 489 (2009).
[58] R. Qiao, T. Chin, S. J. Harris, S. Yan, and W. Yang, Curr. Appl. Phys. **13**, 544 (2013).
[59] A. Ramírez, P. Hillebrand, D. Stellmach, M. M. May, P. Bogdanoff, and S. Fiechter, J. Phys. Chem. C **118**, 14073 (2014).
[60] V. Celorrio, L. Calvillo, G. Granozzi, A. E. Russell, and D. J. Fermin, Top. Catal. **61**, 154 (2018).
[61] F. Wunderlich, T. Leisegang, T. Weißbach, M. Zschornak, H. Stöcker, J. Dshemuchadse, A. Lubk, T. Führlich, E. Welter, D. Souptel, S. Gemming, G. Seifert, and D. C. Meyer, Phys. Rev. B **82**, 014409 (2010).
[62] M. Diaz-Lopez, M. Freire, Y. Joly, C. V. Colin, H. E. Fischer, N. Blanc, N. Boudet, V. Pralong, and P. Bordet, Chem. Mater. **30**, 3060 (2018).
[63] F. Farges, Phys. Rev. B **71**, 155109 (2005).
[64] B. Gilbert, B. H. Frazer, A. Belz, P. G. Conrad, K. H. Nealson, D. Haskel, J. C. Lang, G. Srajer, and G. D. Stasio, J. Phys. Chem. A **107**, 2839 (2003).
[65] W. Schmidt, P. Bottke, M. Sternad, P. Gollob, V. Hennige, and M. Wilkening, Chem. Mater. **27**, 1740 (2015).
[66] S. Ganapathy, A. Vasileiadis, J. R. Heringa, and M. Wagemaker, Adv. Energy Mater. **7**, 1601781 (2017).
[67] H. H. Heenen, C. Scheurer, and K. Reuter, Nano Lett. **17**, 3884 (2017).
[68] A. I. Frenkel, D. M. Pease, J. I. Budnick, P. Metcalf, E. A. Stern, P. Shanthakumar, and T. Huang, Phys. Rev. Lett. **97**, 195502 (2006).